ROYAL SOCIETY
OF CHEMISTRY

PAPER

Check for updates

Influence of alkyl chain length on the photovoltaic properties of dithienopyran-based hole-transporting materials for perovskite solar cells†

Mauricio Caicedo-Reina,‡[a] Manuel Pérez-Escribano, [iD] ‡[b] Javier Urieta-Mora, [iD][cd] Inés García-Benito, [iD][cd] Joaquín Calbo, [iD][b] Alejandro Ortiz, [iD][ae] Braulio Insuasty [iD] *[ae] Agustín Molina-Ontoria, [iD] *[d] Enrique Ortí [iD] *[b] and Nazario Martín [iD] *[cd]

A tailored design of asymmetric hole-transporting materials (HTMs) is reported with the synthesis of a family of new HTMs based on the use of the 5*H*-dithieno[3,2-*b*:2′,3′-*d*]pyran (DTP) moiety endowed with donor *p*-methoxytriphenylamines. A complete experimental and theoretical characterization of the optoelectronic, electrochemical and thermal properties is presented, showing more marked differences in the latter prompted by the different length of the alkyl chains (ethyl, butyl or hexyl) attached to the DTP core. This chemical design plays an important role in the morphological behavior of the new HTMs, displaying a different ability for the deposition on the top surface of the perovskite layer in perovskite solar cells (PSCs), as evidenced by scanning electron microscopy. The photovoltaic performance of the new DTP-based HTMs is highly affected by this morphological behavior, resulting in a maximum power conversion efficiency (PCE) of 17.39% for the ethyl derivative (**DTPA-Et**) in planar devices in combination with the state-of-the-art triple cation perovskite [(FAPbI$_3$)$_{0.87}$(MAPbBr$_3$)$_{0.13}$]$_{0.92}$[CsPbI$_3$]$_{0.08}$. Otherwise, the hexyl derivative (**DTPA-Hex**) showed a decreased value of PCE of 15.04% due to its higher dispersity in chlorobenzene, resulting in a less uniform and lower quality film. In comparison, the reference cell using spiro-OMeTAD reaches a maximum PCE of 18.06%. This work demonstrates that DTP is a good candidate for the preparation of HTMs with high hole mobilities for exploitation in efficient and stable PSCs.

10th Anniversary Statement

Since my previous experience as the Editor-in-Chief of the three Journals of Materials Chemistry A, B and C, their respective impact factors have continuously grown to reach the current remarkable values. This is a direct consequence of the quality of the papers published, mostly on cutting-edge topics related with materials science. Something in which all scientists publishing in Journal of Materials Chemistry agree, is the singularity of these journals in considering the materials science from a chemical perspective. This rather unique approach paves the way of the chemical community to the broad field of materials science, divided in three journals with different and complementary topics. On these bases, I have no doubt about the promising future for the three journals, whose number of papers and engaged scientists is increasing in a regular manner. Guided by the experience and scientific tradition of the Royal Society of Chemistry, the fate of Journal of Materials Chemistry is in the hands of the scientists and, particularly, in their imagination, which is at the forefront of all ventures. My sincere congratulations for this highly celebrated 10th anniversary!

[a] Grupo de Investigación de Compuestos Heterocíclicos, Departamento de Química, Facultad de Ciencias Naturales y Exactas, Universidad del Valle, Calle 13 #100-00, 25360, Cali, Colombia. E-mail: braulio.insuasty@correounivalle.edu.co

[b] Instituto de Ciencia Molecular, Universidad de Valencia, Catedrático José Beltrán 2, 46980, Paterna, Spain. E-mail: enrique.orti@uv.es

[c] IMDEA-Nanociencia, C/Faraday 9, Ciudad Universitaria de Cantoblanco, 28049, Madrid, Spain

[d] Departamento de Química Orgánica, Facultad C. C. Químicas, Universidad Complutense de Madrid, Av. Complutense s/n, 28040, Madrid, Spain. E-mail: nazmar@ucm.es, amolinao@ucm.es; Web: https://ucm.es/info/fullerene/

[e] Center for Research and Innovation in Bioinformatics and Photonics-CIBioFi, Calle 13 #100-00, Edificio E-20, No. 1069, 25360, Cali, Colombia

† Electronic supplementary information (ESI) available. See DOI: https://doi.org/10.1039/d2tc05468j

‡ These authors have contributed equally to the work.

Introduction

Over the past few decades, one of the main challenges for many researchers is to find and develop new technologies that are capable of meeting global energy demand. Considering that the sun provides a huge amount of energy daily, it is postulated as one of the most powerful and attainable sources of energy for the future. Although the global solar energy production is still dominated by silicon solar cells, perovskite solar cells (PSCs) have emerged as a promising technology, achieving an efficiency of 25.7% in a short time.[1] The development of PSCs, from the first report by Miyasaka and coworkers back in 2009 with a power conversion efficiency (PCE) of 3.8%,[2] has relied on the outstanding intrinsic properties that hybrid organic–inorganic perovskites show. These hybrid materials exhibit strong capacity for collecting sunlight in the visible-to-near-IR range,[3] adjustable band gap,[4] long exciton diffusion length (100 nm to 1 μm) and good processability from solution.[5] The chemical composition ABX_3 of hybrid perovskites contains an A cation, which is usually a small organic cation such as methyl ammonium (MA) or formamidinium (FA), a B cation, which often corresponds to Pb^{2+} or Sn^{2+}, and an X anion, which is a halogen (Cl^-, Br^- or I^-).[6] Due to the excellent charge carrier mobility exhibited by perovskites for both electrons and holes, they are typically sandwiched between an electron-transporting layer, such as the inorganic oxides TiO_2 or SnO_2, and a hole-transporting material (HTM). As the hole-transport layer, the most commonly used material is 2,2′,7,7′-tetrakis(N,N-di-p-methoxyphenylamine)-9,9′-spirobifluorene, named as spiro-OMeTAD.[7,8] Despite its excellent performance in combination with perovskite materials, the large-scale use of spiro-OMeTAD is restricted by its considerably high commercial price, motivating the development of alternative HTMs ranging from inorganic to polymeric materials.[9,10] Nevertheless, small organic molecules present some advantages as HTMs, such as its well-defined chemical structure, simpler and more controllable chemical synthesis, easy modification of its properties through chemical design, and processability from solution. In recent years, a wide number of organic molecules has been reported using spiro-based structures, heterocyclic-based scaffolds and donor–acceptor systems, reaching PCE values comparable to those attained with the reference spiro-OMeTAD.[11,12]

Focusing on polycyclic aromatic hydrocarbon structures (PAHs), the incorporation of heteroatoms has been widely used in photovoltaic applications, specifically those containing sulfur in their structure.[11,13–15] This type of compounds usually combines π–π interactions due to their planarity and S···S interactions, leading to an enhancement of conductivity in PSCs.[16,17] Furthermore, the incorporation of sulfur atoms in the structure of the HTMs has been described as a successful approach for enhancing the interaction with the Pb^{2+} cations of the photoactive layer.[18–20] One of the examples of sulfur-containing systems is the 5H-dithieno[3,2-b:2′,3′-d]pyran (DTP) moiety, which provides an interesting core because: (i) the relationship between asymmetry and photovoltaic properties has been little explored,[21,22] the asymmetric DTP can be used as an object of study to more deeply probe the symmetry-
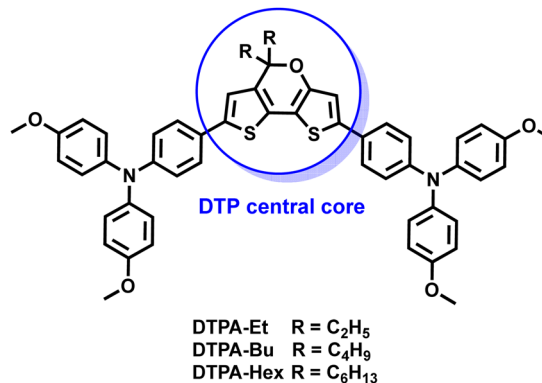

Fig. 1 Chemical structure of the three new HTMs using DTP unit as a central scaffold.

related correlations, and (ii) DTP has a pyran ring, which has been extensively used in dye-sensitized solar cells (DSSCs),[23] organic light-emitting diodes (OLEDs) and non-linear optics.[24] DTP has an oxygen atom that confers electron-rich and high-donating character to the structure with respect to its homologues.[25–27] The use of DTP in photovoltaic applications has been essentially restricted to the preparation of donor polymers.[28–32] The use of small DTP-based molecules in PSCs is also rather limited, although some structural analogues containing the benzodithiophene (BDT),[33] DTP[34] and dithieno[3,2-b:2′,3′-d]thiophene (DTT)[35] cores have been successfully employed to obtain PCEs over 18%.

Here, we report the synthesis of three new HTMs (**DTPA-Et**, **DTPA-Bu** and **DTPA-Hex**) using the DTP moiety as the central core decorated with two p-methoxytriphenylamines (TPA) units and alkyl chains of increasing length (Fig. 1). The structural, electrochemical and optical properties of the synthesized HTMs are fully characterized experimentally, and with the help of first-principles calculations. The new HTMs are successfully incorporated in PSCs using the state-of-the-art triple cation perovskite $[(FAPbI_3)_{0.87}(MAPbBr_3)_{0.13}]_{0.92}[CsPbI_3]_{0.08}$, and the stability and photovoltaic performance of the DTP-based devices are assessed in comparison with spiro-OMeTAD. The effect of increasing the HTM alkyl chain length on the PCE and the charge transport properties is unveiled.

Results and discussion

Synthesis and structural properties of DTPA HTMs

The synthetic procedure for the preparation of the new HTMs based on the DTP central core is outlined in the ESI† (Scheme S1). The starting material **2**, used to obtain the DTP core, was obtained according to previously established synthetic procedures.[32,36] The introduction of the alkyl chains was carried out using different Grignard reagents, leading to the formation of the **3a–c** derivatives, which afforded the DTP core decorated with different alkyl chains (**4a–c**) through dehydration in acid conditions. Selective α-bromination of the thiophene moieties and subsequent two-fold cross-coupling Suzuki reaction with the boronic ester of p-methoxytriphenylamine afforded DTPA-R HTMs (R = Et, Bu, Hex) with good yields of 57, 59 and 54%, respectively. Although the
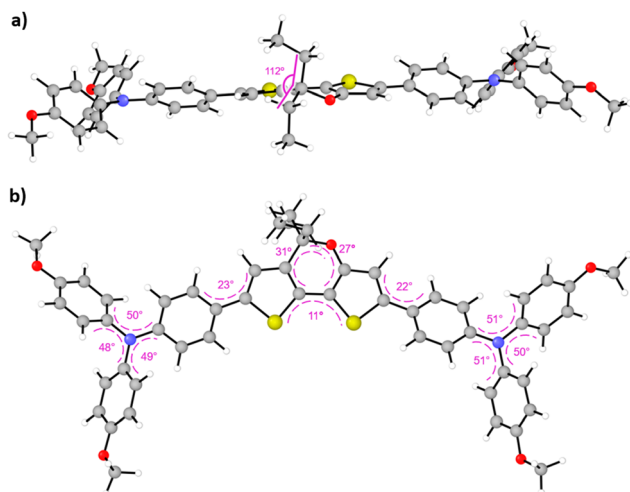
Fig. 2 Side (a) and top (b) views of the minimum-energy structure of **DTPA-Et** calculated at the BMK/6-311G(d,p) level of theory (in CH$_2$Cl$_2$). Characteristic bond angles and dihedral angles are given (see Table S1 and Fig. S1 in the ESI† for **DTPA-Bu** and **DTPA-Hex**).

complete synthesis of the new HTMs requires five synthetic steps, most of the reactions take place at low temperatures, which reduces the cost of the synthesis. The complete HTMs structural characterization was carried out using conventional techniques, such as ^{1}H and ^{13}C NMR, FTIR and high-resolution mass spectrometry, which confirmed the presence of the new compounds (for more details, see the ESI†).

The minimum-energy geometries of the newly synthesized HTMs were theoretically obtained upon full atomic relaxation under the density functional theory (DFT) framework using the BMK/6-311G(d,p) level of theory[37] and CH$_2$Cl$_2$ as solvent (see the ESI† for further details).[38,39] As expected, the calculated DFT-optimized molecular structures of the three DTPA HTMs are very similar to each other. The largest difference was found for the molecular volume, which increases from 809 to 878 and to 947 Å^3 as the length of the alkyl chains attached to the DTP core increases from ethyl (**DTPA-Et**) to butyl (**DTPA-Bu**) and to hexyl (**DTPA-Hex**), respectively. The aliphatic chains are oriented orthogonal to the molecular plane in all cases, with a C(chain)–C(pyran)–C(chain) angle of 112° (Fig. 2a). The pyran core is characterized by an out-of-plane displacement of the O and C(sp^3) atoms with respect to the DTP skeleton (dihedral angles of 27 and 31°, respectively, as indicated in Fig. 2b). The TPA substituents are slightly rotated by around 20° with respect to the molecular plane of the thiophene rings. The TPAs adopt the typical propeller-like structure, in which the dihedral angles between the phenyl groups around the N atom are calculated at *ca.* 50° (Fig. 2b). The high structural similarity is confirmed by the small values found for the root-mean-square deviation when comparing the atomic positions (excluding the alkyl chains): 0.03 and 0.05 Å for **DTPA-Bu** and **DTPA-Hex**, respectively, in comparison with **DTPA-Et**, and 0.04 Å between **DTPA-Bu** and **DTPA-Hex**. The values of the most relevant structural parameters for the three DTPA HTMs are summarized in Fig. S1 and Table S1 in the ESI.†

Electronic, optical and electrochemical properties

Electronic structure calculations were performed at the DFT-BMK/6-311G(d,p) level in CH$_2$Cl$_2$ to unveil the nature of the frontier molecular orbitals for our HTM derivatives (see Fig. 3 for **DTPA-Et**, and Fig. S2 and S3 in the ESI† for **DTPA-Bu** and **DTPA-Hex**, respectively). The highest-occupied molecular orbital (HOMO) spreads over the DTP core with a significant contribution of the TPA moieties. In contrast, the HOMO−1 is mainly located at the TPA units, whereas the HOMO−2 splits into contributions from the external TPAs and the DTP core. The lowest-unoccupied molecular orbital (LUMO) and LUMO+1 are centered over the DTP core with a strong contribution of the inner phenyl ring of the TPAs, whereas the LUMO+2 is localized on the TPA units. The HOMO and LUMO levels are calculated at −5.22 and −1.13 eV, respectively, for the three HTMs (Table S2, ESI†), thus confirming the negligible effect of the alkyl chains on the electronic structure. The HOMO is very close in energy to that calculated for the reference spiro-OMeTAD (−5.18 eV) at the same level of theory, but the LUMO is largely stabilized with respect to the LUMO of spiro-OMeTAD (0.01 eV). The HOMO–LUMO energy gap is therefore predicted to be 4.09 eV for the three DTPA HTMs, significantly smaller than that of spiro-OMeTAD (5.19 eV), suggesting the presence of low-lying excitations in the UV-Vis range.

To evaluate the optical properties of the new HTMs, the UV-Vis absorption and fluorescence emission spectra were recorded using CH$_2$Cl$_2$ as solvent (Fig. 4a). The corresponding optical characteristics are summarized in Table 1. The three HTMs display a broad absorption band around 450 nm, and an emission band with maximum at 495 nm for **DTPA-Et** and **DTPA-Bu**, and at 496 nm for **DTPA-Hex**. The optical band gap (E^{0-0}), estimated at the intersection of the absorption and emission spectra, shows a value of 2.57 eV for all HTMs, which is notably lower than that recorded for spiro-OMeTAD (3.05 eV).

To shed light into the nature of the electronic transitions that shape the absorption spectrum of the DTP-based HTMs, theoretical calculations were performed at the BMK/6-311G(d,p) level (in CH$_2$Cl$_2$) under the time-dependent DFT (TD-DFT) formalism using the previously optimized structures. Theoretical calculations predict an intense (oscillator strength f = 2.0), low-lying singlet excited state S$_1$ at 2.73 eV (*ca.* 454 nm) for the three HTMs (Table 2 and Table S3 in the ESI†), which is unequivocally assigned to the experimental absorption band centered at *ca.* 450 nm (Fig. 4a). This electronic transition is mainly described by the HOMO → LUMO monoexcitation (71%). Based on the topology of the frontier molecular orbitals discussed above, it presents a moderate charge-transfer (CT) character that is reinforced by the contribution of monoexcitations from HOMO−1 and HOMO−2 to LUMO+1 (Table 2 for **DTPA-Et**, Table S3 for **DTPA-Bu** and **DTPA-Hex**, and Fig. S4–S6 (ESI†) for the theoretical convoluted spectra). A detailed study about the CT character of the S$_0$ → S$_1$ excitation can be found in the ESI† (Section S3.4). The deeper, well-defined absorption signal recorded at *ca.* 300 nm is attributed to a combination of high-energy singlet excited states, mostly S$_5$ and S$_8$–S$_{11}$ (Table 2, Table S3 and

This journal is © The Royal Society of Chemistry 2023

J. Mater. Chem. C, 2023, **11**, 8223–8230 | **8225**

Fig. 3 Topology of the frontier molecular orbitals (FMOs) calculated for **DTPA-Et**.

Fig. 4 (a) UV-Vis absorption spectra (solid line) and fluorescence emission spectra (dashed line) of DTP-based HTMs in CH₂Cl₂. (b) Cyclic voltammetry of DTP-based HTMs recorded in CH₂Cl₂ containing 0.1 M tetrabutylammonium hexafluorophosphate (TBAPF₆) at a scan rate of 100 mV s⁻¹. (c) TGA curves recorded for DTP-based HTMs under nitrogen at a heating rate of 10 °C min⁻¹. (d) DSC curves of DTP-based HTMs under nitrogen at a heating rate of 20 °C min⁻¹ (second cycle).

Fig. S4–S6, ESI†). The weak signal in between the largest absorption peaks recorded experimentally at *ca.* 360 nm coincides with the excitation to the second singlet excited state S₂, computed at 3.42 eV (λ = 363 nm; f = 0.24) for the three compounds, which has a DTP-centered nature with a certain contribution of TPA-to-DTP charge transfer. Overall, the simulated absorption

spectra obtained upon convolution of the singlet excited states with Gaussian functions (full-width at half maximum of 0.40 eV) nicely correlate with the experimental data (compare Fig. S4–S6, ESI† and Fig. 4a).

The electrochemical properties of the three HTMs were studied by cyclic voltammetry in nitrogen-purged CH₂Cl₂ solutions at a

8226 | *J. Mater. Chem. C*, 2023, **11**, 8223–8230

This journal is © The Royal Society of Chemistry 2023

Table 1 Optical and electrochemical properties of DTP-based HTMs and spiro-OMeTAD

HTM	$\lambda_{\text{max,abs}}$ [nm]	$\lambda_{\text{max,em}}$ [nm]	$E^{0\text{-}0}$ [eV]	$E^{\text{ox}}_{1/2}$ [V]	E_{HOMO} [eV]	E_{LUMO} [eV]
DTPA-Et	451	495	2.57	0.59	−5.03	−2.46
DTPA-Bu	450	495	2.57	0.57	−5.01	−2.44
DTPA-Hex	452	496	2.57	0.61	−5.05	−2.48
spiro-OMeTAD	386	419	3.05	0.72	−5.16	−2.11

[a] λ_{max} of absorption and emission were measured in CH_2Cl_2 solutions. [b] $E^{0\text{-}0}$ was determined at the intersection of normalized absorption and emission spectra. [c] Determined from CV measurements versus normal hydrogen electrode (NHE). [d] E_{HOMO} is estimated in eV by $E_{\text{HOMO}} = -4.44\text{ eV} - E^{\text{ox}}_{1/2}$. [e] E_{LUMO} were estimated by $E_{\text{LUMO}} = E_{\text{HOMO}} + E^{0\text{-}0}$.

Table 2 Excitation energies (in eV and nm), oscillator strengths (f) and description in terms of molecular orbitals calculated for some of the lowest-energy singlet excited states (S_n) of **DTPA-Et** at the BMK/6-311G(d,p) level of theory in CH_2Cl_2. H and L correspond to HOMO and LUMO, respectively

State	E (eV)	λ (nm)	f	Monoexcitation	%
S$_1$	2.73	454	2.01	H → L	71
				H−1 → L+1	16
				H−2 → L+1	13
S$_2$	3.42	363	0.24	H−1 → L	64
				H → L+1	36
S$_5$	3.85	322	0.24	H−2 → L	54
				H−1 → L+1	24
				H → L+1	12
S$_9$	4.38	283	0.39	H−2 → L+7	44
				H−1 → L+7	38
				H → L+7	18

scan rate of 100 mV s^{-1} (Fig. 4b). The corresponding first oxidation potentials are summarized in Table 1. The three new HTMs show a similar redox behavior with three reversible oxidations, with the first half-wave potential in the range of 0.57–0.61 V. The HOMO energy levels are estimated at −5.03, −5.01 and −5.05 eV for **DTPA-Et**, **DTPA-Bu** and **DTPA-Hex**, respectively, exhibiting a slightly stronger donor ability in comparison to spiro-OMeTAD measured under similar conditions (−5.16 eV).[22] Therefore, the new HTMs offer a good alignment between their HOMO levels and the valence band edge of the triple cation perovskite $[[(FAPbI_3)_{0.87}(MAPbBr_3)_{0.13}]_{0.92}[CsPbI_3]_{0.08}$ situated at −5.70 eV, which points to an efficient injection of holes from the HTM to the perovskite. The energy levels of the different constituents of the PSC are schematically illustrated in Fig. S13 (ESI†). As well as for the optical properties, no significant influence is observed on the redox properties upon variation of the length of the alkyl chain attached to the DTP core.

The adiabatic ionization energies up to the third oxidation were theoretically calculated for the DTP-based HTMs at the BMK/6-311G(d,p) level of theory in CH_2Cl_2. The first ionization energy (IE$_1$, neutral to radical cation) indicates that **DTPA-Et**, **DTPA-Bu** and **DTPA-Hex** are oxidized more easily than spiro-OMeTAD, with IE$_1$ values of 4.58 eV for **DTPA-Et** and of 4.57 eV for **DTPA-Bu** and **DTPA-Hex**, to be compared with an IE$_1$ of 4.66 eV for spiro-OMeTAD. This trend is in good agreement

with that observed for the first experimental $E^{\text{ox}}_{1/2}$ value (Table 1), confirming the stronger electron-donating nature of the DTP-based HTMs compared to spiro-OMeTAD. The second ionization energy (cation to singlet dication) is predicted at 5.06 eV for the three HTMs, ca. 0.5 eV larger in energy than IE$_1$, thus supporting the presence of two near, still differentiated, one-electron oxidation peaks recorded at 0.6–0.8 V in the voltammetry experiments (Fig. 4b). The formation of the radical trication is determined by an IE$_3$ of 5.44 eV for **DTPA-Et** and **DTPA-Bu,** and of 5.43 eV for **DTPA-Hex**. The origin of the oxidation processes is disentangled by analyzing the Mulliken net charges accumulated by the different fragments constituting the HTMs for the charged species (Fig. S9 and Table S4, ESI†). Theoretical calculations indicate that the first and second oxidation processes correspond to one-electron extractions involving both the DTP core and the TPA units (as expected from the HOMO topology, see Fig. 3), with an increase in the net charge of +0.46e for DTP and +0.54e for TPAs in going from neutral to cation, and of +0.30e for DTP and +0.70e for TPAs from cation to dication. In contrast, the third oxidation takes place mainly over the TPA moieties, which increase their total net charge by +0.96e compared to the dication species.

Thermal properties

The thermal behavior of the new DTP-based HTMs was characterized using standard techniques such as thermogravimetric analysis (TGA) and differential scanning calorimetry (DSC) (Fig. 4c and d, respectively). DSC analysis provides more insight into the morphological behavior of the new HTMs. The three HTMs display a different thermal behavior owing to the different length of the alkyl chains incorporated in the structure. **DTPA-Et**, **DTPA-Bu** and **DTPA-Hex** essentially show an amorphous character and only a low glass transition at 106, 77, and 55 °C, respectively, is detected (Fig. S10–S12, ESI†).

Photovoltaic results

The new dithienopyran-based molecules were tested as HTMs in planar solution-processed PSCs. The devices were fabricated from a stack of thin films onto indium tin oxide (ITO) conductive glass. The device configuration employed in this work is the standard ITO/SnO$_2$/Perovskite/HTM/Au, incorporating the state-of-the-art triple cation $[[(FAPbI_3)_{0.87}(MAPbBr_3)_{0.13}]_{0.92}[CsPbI_3]_{0.08}$ perovskite. Details regarding cell fabrication are included in the ESI.† The cross-section scanning electron microscopy (SEM) images of the devices are shown in Fig. S14 (ESI†). Despite the excellent solubility of the new HTMs in chlorobenzene, the cross-sectional images show differences in the average HTM thickness being 93, 75, 48 and 137 nm for **DTPA-Et**, **DTPA-Bu**, **DTPA-Hex** and spiro-OMeTAD, respectively. The top view of the SEM images (Fig. S15 and S16, ESI†) show a good film formation in the case of **DTPA-Et** and **DTPA-Bu**. In contrast, **DTPA-Hex** showed thinner films with lower uniformity and surface coverage, which resulted in the formation of pinholes (Fig. S16, ESI†).

The current density–voltage (J–V) characteristics, measured for the best-performing devices under 1 Sun AM 1.5 G (100 mW cm^{-2}) simulated sunlight, are illustrated in Fig. 5a, and the corresponding
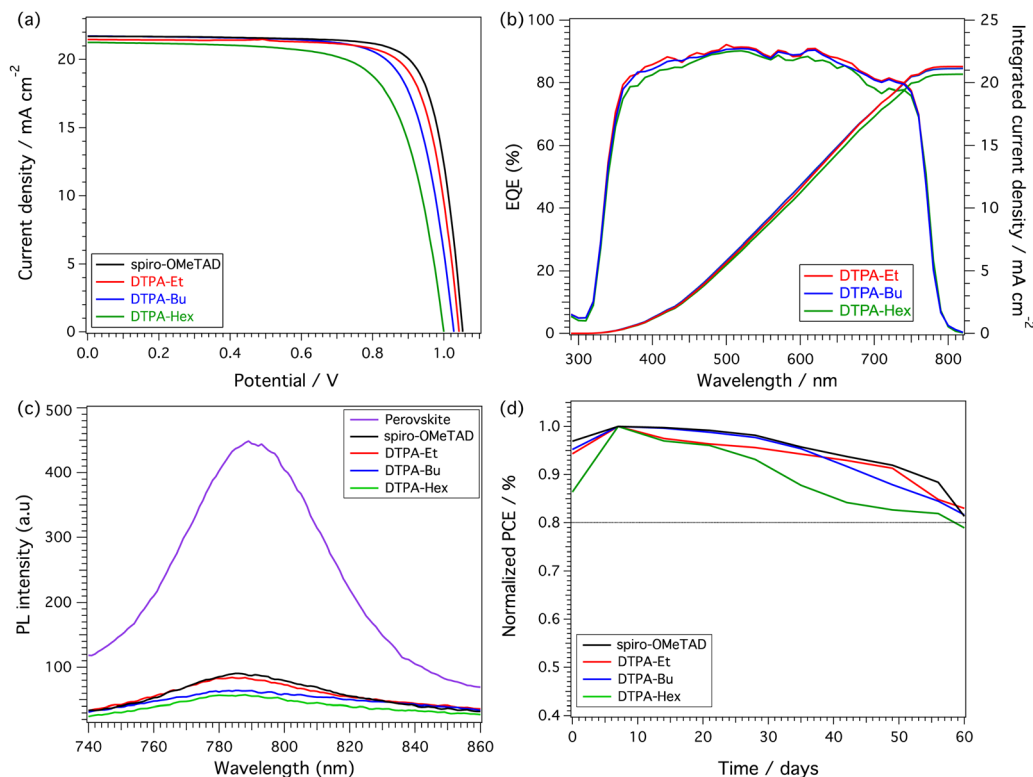
Fig. 5 (a) Current density–voltage (J–V) curves of DTPA HTMs in planar $[(FAPbI_3)_{0.87}(MAPbBr_3)_{0.13}]_{0.92}[CsPbI_3]_{0.08}$-based devices. (b) External quantum efficiency (EQE) plots of DTPA HTMs with the corresponding integrated current. (c) Steady-state PL spectra of the pristine triple cation perovskite and perovskite/HTM films. (d) Stability test of the unencapsulated devices incorporating DTPAs and spiro-OMeTAD as HTMs stored in an ambient atmosphere at room temperature with a relative humidity of 30%.

photovoltaic parameters are summarized in Table 3. Ethyl-substituted DTPA (**DTPA-Et**) devices showed the best efficiencies, exhibiting a maximum PCE of 17.39% with an open-circuit voltage (V_{OC}) of 1.04 V, a short-circuit current (J_{SC}) of 21.47 mA cm^{-2}, and a fill factor (FF) of 77.70%. A slightly lower efficiency was measured for the devices based on the butyl-substituted DTPA (**DTPA-Bu**), which reached a maximum PCE of 16.82% owing to the decreased values of J_{SC} (21.34 mA cm^{-2}) and FF (75.40%). Finally, the hexyl-derivative (**DTPA-Hex**) showed the lowest efficiency values (a maximum PCE of 15.04%) as a consequence of the reduced V_{OC}, J_{SC} and FF. In all cases, the maximum PCEs measured for the DTPA HTMs are lower than those obtained for the reference spiro-OMeTAD (Table 3), which achieved a PCE of 18.06% in correlation with the enhanced values of V_{OC} (1.05 V), J_{SC} (21.70 mA cm^{-2}) and FF (79.70%). In all cases, the devices containing both DTP-based and spiro-OMeTAD HTMs showed almost negligible hysteresis (Fig. S17, ESI†). The

statistics obtained for 10 devices of each HTM are summarized in Fig. S18 and Table S5 (ESI†), showing a good reproducibility, especially in the case of the ethyl-derivative, as expected for the better homogeneity of the devices that incorporate this HTM.

To assess the hole extraction ability of **DTPA-Et**, **DTPA-Bu** and **DTPA-Hex**, the steady-state photoluminescence (PL) was recorded (Fig. 5c). The pristine perovskite film shows a strong PL signal centered at 790 nm, which stems from the radiative recombination of the photogenerated charge carriers. After the deposition of the HTMs on the perovskite surface, the PL signal intensity decreases significantly in all cases. This quenching probes the effective hole extraction achieved upon the HTM deposition. Fig. 5b displays the external quantum efficiencies (EQEs) and the integrated photocurrent calculated for the new DTP-based HTMs, which are in good agreement with those obtained from the J–V measurements. The charge transport and hole collection properties of the new HTMs and spiro-OMeTAD were determined on hole-only devices (μ_h) using the space-charge limited current method (SCLC) (Fig. S22 and Table S6 in the ESI†). Although the mobility of **DTPA-Et** (2.53×10^{-4} cm^2 V^{-1} s^{-1}) and **DTPA-Bu** (1.11×10^{-4} cm^2 V^{-1} s^{-1}) are slightly lower than that measured for spiro-OMeTAD (4.41×10^{-4} cm^2 V^{-1} s^{-1}), an efficient charge transport is expected. However, the mobility of **DTPA-Hex** (7.41×10^{-5} cm^2 V^{-1} s^{-1}) is almost one order of magnitude lower than for spiro-OMeTAD, which clearly justifies its poorer performance. Therefore, the hole mobility of the doped-

Table 3 Maximum device performance of DTP-based HTMs and spiro-OMeTAD in combination with the $[(FAPbI_3)_{0.87}(MAPbBr_3)_{0.13}]_{0.92}[CsPbI_3]_{0.08}$ perovskite

HTM	V_{OC} (V)	J_{SC} (mA cm^{-2})	FF (%)	PCE (%)
DTPA-Et	1.04	21.47	77.70	17.39
DTPA-Bu	1.04	21.34	75.40	16.82
DTPA-Hex	1.00	21.25	70.83	15.04
spiro-OMeTAD	1.05	21.70	79.10	18.06

HTMs follows the same tendency as the *J–V* measurements. The better hole mobilities and morphology of the spiro-OMeTAD films contribute to the slightly higher FF and PCE obtained for spiro-OMeTAD-based devices compared with DTPA devices. Theoretical gas-phase reorganization energies upon one-electron extraction (λ_h, see the ESI† for details) support the lower hole-transport ability of the DTPA HTMs, with λ_h of 0.52 eV for **DTPA-Et**, **DTPA-Bu** and **DTPA-Hex** compared to a value of 0.45 eV for spiro-OMeTAD at the same level of theory (BMK/6-311G(d,p)). The longer alkyl chains in **DTPA-Hex** might lead to longer (less efficient) charge-carrier hops and/or lower uniformity in the molecular packing, thus causing its poorer charge transport properties.

We finally evaluated the stability of the devices without encapsulation containing the new DTP-based HTMs under ambient conditions and dark storage (RT, RH 30 ± 5%) as depicted in Fig. 5d. The new **DTPA-Et** and **DTPA-Bu** HTMs show promising stability in dark storage, maintaining more than 80% of the maximum efficiency after 60 days. The evolution of the efficiency of DTPA-based devices was monitored under continuous 1 Sun illumination. After 5 hours, **DTPA-Hex** shows a decrease in the efficiency of almost 10% of the original values (Fig. S19, ESI†). In comparison, devices based on **DTPA-Et**, **DTPA-Bu** and spiro-OMeTAD maintain 95% of their initial PCE. Additionally, the thermal stability of the devices was explored by applying thermal annealing at 60 °C and 85 °C (30% relative humidity, RH) for 1 h (Fig. S20 and S21, ESI†). Upon thermal stress at 60 °C, a more significant degradation was observed after 20 minutes, especially for devices with **DTPA-Hex** and **DTPA-Bu**. At 85 °C, the degradation of all HTMs, including spiro-OMeTAD, is remarkable, dropping to 25% (**DTPA-Hex**), 33% (**DTPA-Bu**), 46% (**DTPA-Et**) and 55% (spiro-OMeTAD) of their initial performance.

Conclusions

We have designed, synthesized and studied the optical, electronic and thermal properties of three hole-transporting materials featuring 5*H*-dithieno[3,2-*b*:2′,3′-*d*]pyran (DTP) as a central core endowed with *p*-methoxytriphenylamines. The structural, optical, electrochemical and thermal properties of the new HTMs have been characterized experimentally and with DFT calculations. The influence of the length of the alkyl chains (ethyl, butyl or hexyl) attached to the central scaffold has been analyzed. As expected, the optoelectronic features remain mostly unaffected by increasing the length of the alkyl chain, whereas more relevant changes are observed in the thermal properties. The DTP-based HTMs were incorporated in planar PSCs using $[(FAPbI_3)_{0.87}(MAPbBr_3)_{0.13}]_{0.92}[CsPbI_3]_{0.08}$ as the photoactive layer. **DTPA-Hex** reached a maximum PCE of only 15.04%, which is attributed to the lower uniformity of the spin-coated layer that enhances the interfacial charge recombination and also to its poorer charge-transport properties. Under the same conditions, **DTPA-Et** and **DTPA-Bu** yielded PCEs up to 17.39% and 16.82%, respectively. The maximum PCEs reached by the new HTMs are slightly lower compared to that achieved by the reference spiro-OMeTAD (18.06%), but present promising stability under dark storage and ambient conditions.

Conflicts of interest

There are no conflicts to declare.

Acknowledgements

References

1 N. R. E. L. National Renewable Energy Laboratory, https://www.nrel.gov/ncpv/images/efficiency_chart.jpg, (accessed Janurary, 2023).

2 A. Kojima, K. Teshima, Y. Shirai and T. Miyasaka, *J. Am. Chem. Soc.*, 2009, **131**, 6050–6051.

3 P. Qin, S. Paek, M. I. Dar, N. Pellet, J. Ko, M. Grätzel and M. K. Nazeeruddin, *J. Am. Chem. Soc.*, 2014, **136**, 8516–8519.

4 K. Do, H. Choi, K. Lim, H. Jo, J. W. Cho, M. K. Nazeeruddin and J. Ko, *Chem. Commun.*, 2014, **50**, 10971–10974.

5 L. Fagiolari and F. Bella, *Energy Environ. Sci.*, 2019, **12**, 3437–3472.

6 R. Wang, M. Mujahid, Y. Duan, Z.-K. Wang, J. Xue and Y. Yang, *Adv. Funct. Mater.*, 2019, **29**, 1808843.

7 Z. Yu and L. Sun, *Adv. Energy Mater.*, 2015, **5**, 1500213.

8 M. Saliba, T. Matsui, J.-Y. Seo, K. Domanski, J.-P. Correa-Baena, M. K. Nazeeruddin, S. M. Zakeeruddin, W. Tress, A. Abate, A. Hagfeldt and M. Gratzel, *Energy Environ. Sci.*, 2016, **9**, 1989–1997.

9 Z. Yu and L. Sun, *Small Methods*, 2018, **2**, 1700280.

10 M. M. H. Desoky, M. Bonomo, N. Barbero, G. Viscardi, C. Barolo and P. Quagliotto, *Polymers*, 2021, **13**, 1652.

11 J. Urieta-Mora, I. García-Benito, A. Molina-Ontoria and N. Martín, *Chem. Soc. Rev.*, 2018, **47**, 8541–8571.

This journal is © The Royal Society of Chemistry 2023

J. Mater. Chem. C, 2023, **11**, 8223–8230 | **8229**

12 X. Yin, Z. Song, Z. Li and W. Tang, *Energy Environ. Sci.*, 2020, **13**, 4057–4086.

13 I. García-Benito, J. Urieta-Mora, A. Molina-Ontoria and N. Martín, *Bull. Chem. Soc. Jpn.*, 2021, **94**, 1311–1323.

14 I. Garcia-Benito, I. Zimmermann, J. Urieta-Mora, J. Arago, A. Molina-Ontoria, E. Orti, N. Martin and M. K. Nazeeruddin, *J. Mater. Chem. A*, 2017, **5**, 8317–8324.

15 I. García-Benito, I. Zimmermann, J. Urieta-Mora, J. Aragó, J. Calbo, J. Perles, A. Serrano, A. Molina-Ontoria, E. Ortí, N. Martín and M. K. Nazeeruddin, *Adv. Funct. Mater.*, 2018, **28**, 1801734.

16 I. Zimmermann, J. Urieta-Mora, P. Gratia, J. Aragó, G. Grancini, A. Molina-Ontoria, E. Ortí, N. Martín and M. K. Nazeeruddin, *Adv. Energy Mater.*, 2017, **7**, 1601674.

17 J. Urieta-Mora, I. Zimmermann, J. Aragó, A. Molina-Ontoria, E. Ortí, N. Martín and M. K. Nazeeruddin, *Chem. Mater.*, 2019, **31**, 6435–6442.

18 M. Saliba, S. Orlandi, T. Matsui, S. Aghazada, M. Cavazzini, J.-P. Correa-Baena, P. Gao, R. Scopelliti, E. Mosconi, K.-H. Dahmen, F. De Angelis, A. Abate, A. Hagfeldt, G. Pozzi, M. Graetzel and M. K. Nazeeruddin, *Nat. Energy*, 2016, **1**, 15017.

19 Q.-Q. Ge, J.-Y. Shao, J. Ding, L.-Y. Deng, W.-K. Zhou, Y.-X. Chen, J.-Y. Ma, L.-J. Wan, J. Yao, J.-S. Hu and Y.-W. Zhong, *Angew. Chem., Int. Ed.*, 2018, **57**, 10959–10965.

20 M.-H. Li, T.-G. Sun, J.-Y. Shao, Y.-D. Wang, J.-S. Hu and Y.-W. Zhong, *Nano Energy*, 2021, **79**, 105462.

21 X. Wang, A. Tang, Y. Chen, A. Mahmood, J. Hou, Z. Wei and E. Zhou, *RSC Adv.*, 2016, **6**, 90051–90060.

22 J. Urieta-Mora, I. García-Benito, L. A. Illicachi, J. Calbo, J. Aragó, A. Molina-Ontoria, E. Ortí, N. Martín and M. K. Nazeeruddin, *Sol. RRL*, 2021, **5**, 2100650.

23 B. Chu, H. Wang, B. Xerri, K. H. Lee, T. Yang, Z. Wang, Z. Lin, Y. Liang, C. Adamo, S. Yang and J. Sun, *RSC Adv.*, 2014, **4**, 62472–62475.

24 Y. Zhou, M. Li, Y. Guo, H. Lu, J. Song, Z. Bo and H. Wang, *ACS Appl. Mater. Interfaces*, 2016, **8**, 31348–31358.

25 J. W. Jung, T. P. Russell and W. H. Jo, *Chem. Mater.*, 2015, **27**, 4865–4870.

26 X. Wang, A. Tang, F. Chen and E. Zhou, *Polym. Chem.*, 2017, **8**, 5396–5406.

27 S. Wen, Y. Wu, Y. Wang, Y. Li, L. Liu, H. Jiang, Z. Liu and R. Yang, *ChemSusChem*, 2018, **11**, 360–366.

28 J. You, L. Dou, K. Yoshimura, T. Kato, K. Ohya, T. Moriarty, K. Emery, C. C. Chen, J. Gao, G. Li and Y. Yang, *Nat. Commun.*, 2013, **4**, 1446.

29 R. Hünig, A. Mertens, M. Stephan, A. Schulz, B. Richter, M. Hetterich, M. Powalla, U. Lemmer, A. Colsmann and G. Gomard, *Adv. Opt. Mater.*, 2016, **4**, 1487–1493.

30 S. Zhang, L. Zuo, J. Chen, Z. Zhang, J. Mai, T. K. Lau, X. Lu, M. Shi and H. Chen, *J. Mater. Chem. A*, 2016, **4**, 1702–1707.

31 J. You, C. C. Chen, Z. Hong, K. Yoshimura, K. Ohya, R. Xu, S. Ye, J. Gao, G. Li and Y. Yang, *Adv. Mater.*, 2013, **25**, 3973–3978.

32 L. Dou, C. C. Chen, K. Yoshimura, K. Ohya, W. H. Chang, J. Gao, Y. Liu, E. Richard and Y. Yang, *Macromolecules*, 2013, **46**, 3384–3390.

33 R. Sandoval-Torrientes, I. Zimmermann, J. Calbo, J. Aragó, J. Santos, E. Ortí, N. Martín and M. K. Nazeeruddin, *J. Mater. Chem. A*, 2018, **6**, 5944–5951.

34 R. Azmi, S. Y. Nam, S. Sinaga, Z. A. Akbar, C.-L. Lee, S. C. Yoon, I. H. Jung and S.-Y. Jang, *Nano Energy*, 2018, **44**, 191–198.

35 X. Liu, F. Kong, F. Guo, T. Cheng, W. Chen, T. Yu, J. Chen, Z. Tan and S. Dai, *Dyes Pigm.*, 2017, **139**, 129–135.

36 C. Xia, H. Wu, Q. Yue, S. Chen, L. Shui, H. Fan and X. Zhu, *J. Mater. Chem. C*, 2019, **7**, 15344–15349.

37 A. D. Boese and J. M. L. Martin, *J. Chem. Phys.*, 2004, **121**, 3405–3416.

38 A. D. McLean and G. S. Chandler, *J. Chem. Phys.*, 1980, **72**, 5639–5648.

39 R. Krishnan, J. S. Binkley, R. Seeger and J. A. Pople, *J. Chem. Phys.*, 1980, **72**, 650–654.